Heterogenization of Ru(II) polypyridyl photoredox complexes on covalent triazine frameworks

Arthur De Vos,[†] Kurt Lejaeghere,[*,†] Francesco Muniz Miranda,[†] Christian V. Stevens,[‡] Pascal Van Der Voort,[¶] and Veronique Van Speybroeck[*,†]

[†]*Center for Molecular Modeling (CMM), Ghent University, Technologiepark 46, 9052 Zwijnaarde, Belgium*

[‡]*Research Group SynBioC, Department of Green Chemistry and Technology, Faculty of Bioscience Engineering, Ghent University, Campus Coupure, Coupure Links 653 bl. B, 9000 Gent, Belgium*

[¶]*Center for Ordered Materials, Organometallics and Catalysis (COMOC), Department of Inorganic and Physical Chemistry, Ghent University, Krijgslaan 281 (S3), 9000 Gent, Belgium*

E-mail: Kurt.Lejaeghere@UGent.be; Veronique.VanSpeybroeck@UGent.be

Supporting Information

Contents

S1 Structures **2**

S2 Charged systems **3**

S2.1 Energetics 3

S2.2 Alignment 3

S3 Level of theory **6**

S4 The linkers **10**

S4.1 Electronic structure 10

S5 The scaffold **12**

S5.1 Energetics 12

S5.2 Electronic structure 13

S6 The active complex **16**

S6.1 Energetics 16

S6.2 Electronic structure 16

S7 The heterogeneous catalyst **20**

S7.1 Energetics 20

S7.2 Electronic structure 21

S1 Structures

While Ru(II)L_3 complexes can be attached to CTFs in various combinations, only a representative subset was considered to limit the computational load. The calculated structures are summarized in Table S1. The Ru(II)L_3 complexes are listed in Table S1a, the CTFs in Table S1b and the anchored Ru(II)L_3 complexes in Table S1c.

L_2^j \ L^i	Cbipy	Phen	Bipm	Cbipz
Cbipy	✓	✓	✓	✓
Phen	✓	✓	✓	✓
Bipm	✓	✓	✓	✓
Cbipz	✓	✓	✓	✓

(a) Ru(II)L_3

L^i	L_1^ibiph$_2$	L_2^ibiph$_1$	L_3^i
Biph	✓		
Cbipy	✓	✓	✓
Tbipy	✓	✓	✓
Phen	✓	✓	✓
Bipm	✓	✓	✓
Cbipz	✓	✓	✓
Tbipz	✓	✓	✓

(b) CTF

L^i	Ru(II)cbipy$_2$$L_1^i$			Ru(II)phen$_2$$L_1^i$			Ru(II)bipm$_2$$L_1^i$			Ru(II)cbipz$_2$$L_1^i$		
	L_1^ibiph$_2$	L_2^ibiph$_1$	L_3^i	L_1^ibiph$_2$	L_2^ibiph$_1$	L_3^i	L_1^ibiph$_2$	L_2^ibiph$_1$	L_3^i	L_1^ibiph$_2$	L_2^ibiph$_1$	L_3^i
Cbipy	✓	✓	✓	✓			✓			✓	✓	✓
Phen	✓	✓	✓				✓	✓	✓	✓	✓	✓
Bipm	✓	✓	✓							✓	✓	✓
Cbipz	✓	✓	✓									

(c) Ru(II)L_3+CTF

Table S1: Calculated Ru(II)L_3 complexes (Ru(II)$L_2^jL_1^i$) (a), CTFs (L_n^ibiph$_{3-n}, n = 0, 1, 2, 3$) (b) and their combination ((Ru(II)L_2^j)L_1^i(L_n^ibiph$_{2-n}$), $n = 0, 1, 2$) (c).

S2 Charged systems

S2.1 Energetics

Calculating the energy of charged molecules with a periodic code like VASP gives rise to spurious interactions, which need to be corrected. We applied a first-order correction term associated with monopole interactions,[1] i.e. interactions between periodic point charges. The extent to which higher order terms need to be included was assessed by comparing to nonperiodic DFT results. In particular, the electron affinity of divalent Ru(II)cbipy$_3$ complexes was calculated with Gaussian16[2] employing a def2-TZVPP basis set.[3,4] Comparison to VASP predictions using a $40 \times 40 \times 40$ Å^3 unit cell, including the monopole correction, showed a good agreement with a difference of less than 12 meV (see Table S2). Further correction terms are therefore expected to have a small effect and were not included.

L_2^j \ L^i	Cbipy	Phen	Bipm	Cbipz
Cbipy	-6.993	-6.938	-7.232	-7.420
Phen	-6.883	-6.835	-7.110	-7.311
Bipm	-7.837	-7.783	-8.053	-8.245
Cbipz	-7.469	-7.402	-7.705	-7.873

(a) VASP

L_2^j \ L^i	Cbipy	Phen	Bipm	Cbipz
Cbipy	-6.985	6.931	-7.223	-7.412
Phen	-6.879	-6.831	-7.104	-7.305
Bipm	-7.829	-7.775	-8.045	-8.238
Cbipz	-7.459	-7.394	-7.695	-7.864

(b) Gaussian

Table S2: Electron affinities of the RuL_3 complexes (in eV) calculated by VASP (a) and Gaussian (b).

S2.2 Alignment

Also the alignment of the electronic structure is hampered by long-range spurious interactions in charged systems. An alignment based on the vacuum energy, deduced from the electrostatic potential, is only slowly convergent as a function of the unit cell size (see Table S3). Alternatively the vacuum energy can be derived as the sum of the band gap (E_g) and the electron affinity (EA), which is calculated as the energy gained upon adding a supplementary electron. When changing the unit cell dimensions from 20 to 40 Å, this value varies only within 100 meV, while E_{Vac} differs by more than 2 eV (see Table S3). Moreover in the $40 \times 40 \times 40$ Å^3 unit cell, the difference between E_{Vac} and $EA + E_g$ is below 100 meV.

Ru(II)cbipy$_3$	EA	$EA + E_g$	E_{Vac}
$20 \times 20 \times 20$ Å^3	6.859	8.550	7.083
$20 \times 20 \times 40$ Å^3	6.961	8.648	9.751
$40 \times 40 \times 40$ Å^3	6.945	8.656	8.565

Table S3: Comparison of vacuum energies (in eV) based on a direct approach (E_{Vac}) and on the the electron affinity (EA) as a function of the box size. The $20 \times 20 \times 40$ Å^3 unit cell is similar in size as a (Ru(II)cbipy$_2$)cbipy(biph$_2$) catalyst with a vacuum region of 40 Å.

In conclusion, the sum of the electron affinity and the band gap converges much faster with respect to the unit cell size than the vacuum energy. Moreover, irrespective of which value is used, all aligned structures display the same trend (see Fig. S1).

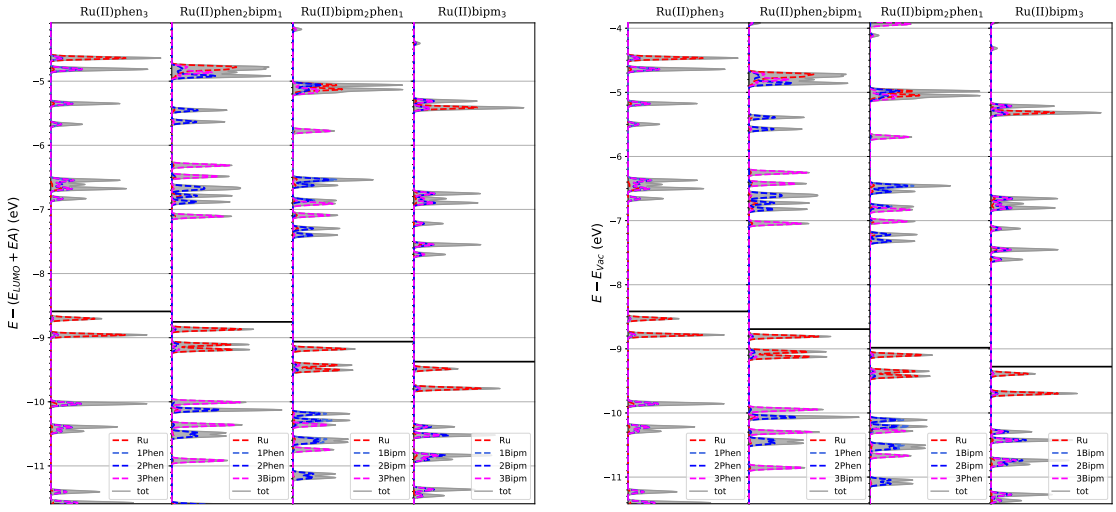

(a) Alignment based on electron affinity

(b) Alignment based on vacuum energy

Figure S1: Densities of states of the Ru(II)L$_2^j$L$_1^i$ (L = bipm, phen) complex aligned using the electron affinity (a) or the vacuum energy (b).

If we want to compare the electronic structures of systems with different charges, the vacuum energy is an unsuitable energy reference as it depend on the total charge. The comparison of the electronic structure of a Ru(II)L$_3$ complex with its linkers (see Figure S10) or the sole scaffold with the Ru(II)L$_3$-CTF catalyst (see Figure S13a) demands a more suitable reference. In those cases the electrostatic potential at an ion is calculated by placing a test charge:

$$\overline{V}_n = \int V(\mathbf{r}) \rho_{test}(|\mathbf{r} - \mathbf{R_n}|) d^3\mathbf{r} \tag{S1}$$

i.e., the average of the electrostatic potential a typical core electron would experience. The integral is calculated over a spherically symmetric region of which the radius is related to the PAW core radius. The norm of the test charge is constrained to one. The radii for the test charge distributions are taken at 0.5883 Å, 0.5902 Å, 0.6991 Å and 0.9685 Å for the hydrogen, nitrogen, carbon and ruthenium atoms respectively. To qualitatively align electronic structures of different systems we average this core potential over all atoms in a common moiety. Note that this approach can also be used for structures with the same charge (see Fig S13b).

S3 Level of theory

In this section we assess the impact of the used functional on the electronic structure by performing selected HSE06 calculations. Further sections are limited to PBE.

The CTF scaffold Figure S2 displays the HSE06 counterpart of the PBE results of Figure 3 of the main article. Similarly to the PBE results the energy and shape of the localized CTF electron states are recovered from the individual linkers. Moreover the CBM systematically decreases if the nitrogenous character of the framework is increased. We therefore conclude that the PBE and HSE06 results yield similar trends.

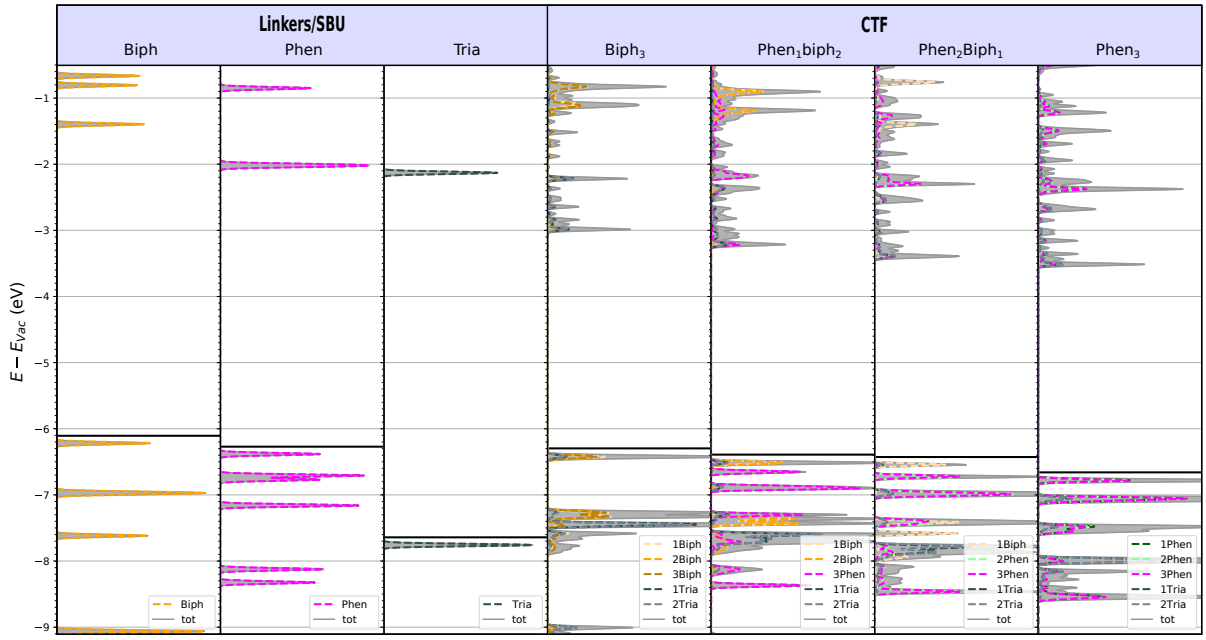

Figure S2: HSE06 densities of states of CTF-1-2R doped with 1, 2 or 3 phenanthroline linkers ($\text{phen}_n\text{biph}_{3-n}, n = 0, 1, 2, 3$) compared to the electronic structure of the hydrogen-terminated constituents (biph, phen, tria). The DOS are aligned with respect to the vacuum energy.

Although the properties of the CTF determined with the PBE or HSE06 functional show a good resemblance, changing the functional from PBE to HSE06 does not remain entirely without consequence. The most prominent effect is the increase in the band gap, expected when using a hybrid functional. A second alteration is visible for the localized occupied states, which change their relative stability. We investigated this further by examining the energy gaps between the LUMO, which has a delocalized character, and the highest occupied (HO) orbital centered on a particular

linker (see Figure S3). Although the individual phen and biph states indeed change order, the linker-centered gaps as a function of the nitrogen content follow the same trend in PBE and HSE06 calculations

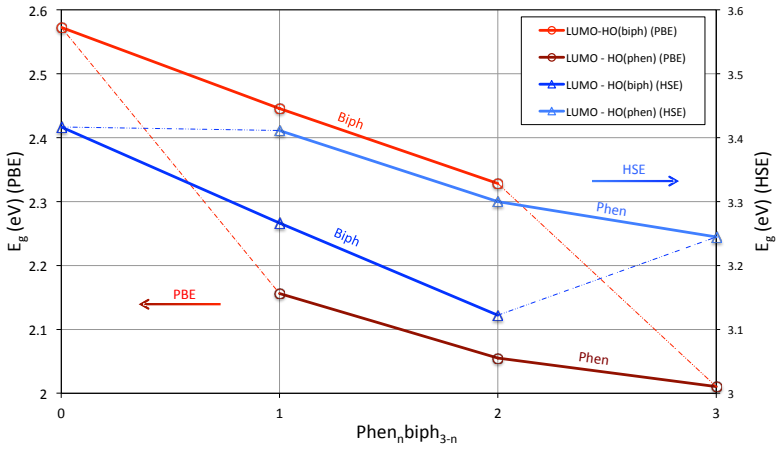

Figure S3: Energy gaps for PBE (red) and HSE06 (blue) calculations of $\text{phen}_n\text{biph}_{3-n}, n = 0, 1, 2, 3$. The energy gaps are defined between the LUMO, which has a delocalized character, and the highest occupied (HO) state localized on either a phen or biph linker.

The Ru(II)L_3 complex Figure S4 compares PBE and HSE06 results for Ru(II)phen$_n$bipm$_{3-n}$ complexes ($n = 0, 1, 2, 3$), which are partly included in Figure 5 of the main manuscript. Besides an increase in band gap, both levels of theory agree excellently.

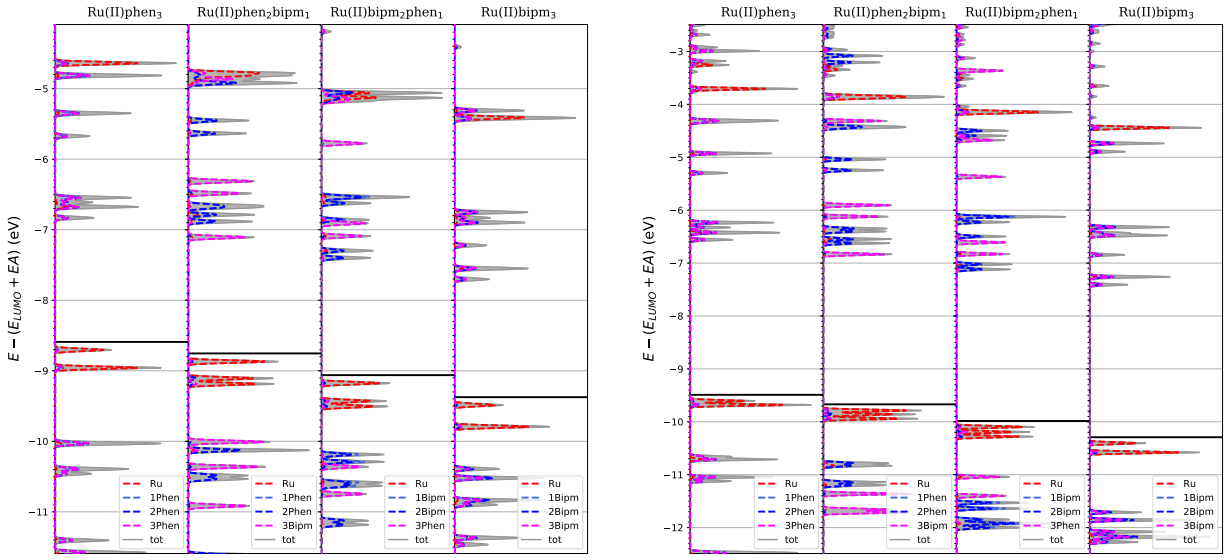

(a) PBE (b) HSE06

Figure S4: Densities of states (PBE, HSE06) of Ru(II)phen$_n$bipm$_{3-n}$ complexes ($n = 0, 1, 2, 3$) aligned using the electron affinity.

The heterogeneous catalyst Last the influence of the level of theory is investigated for the combined Ru(II)L_3-CTF heterogeneous catalyst. Some selected PBE and HSE06 calculations were performed and are shown in Figure S5. Figure S5a can be compared to Figure 6a of the main manuscript, which displays the corresponding PBE data. Again there is a good resemblance between both levels of theory, which is inherited from the separate building blocks, i.e. the scaffold and complex. However changing the functional from PBE to HSE06 does have some influence. The most prominent effect for the Ru(II)L_3-CTF catalyst is the increase in its band gap. A second alteration is visible for the unoccupied states localized on the anchoring linker, as their stability is decreased compared to those centered on the pore. This effect is not strong but can cause the LUMO states to mix different linker states (see Figure S5a) compared to the PBE results (see Figure 6a). A distinct, unidirectional MLCT towards either the pore or framework, as described in the main article, remains possible (see Figures S5b, c).

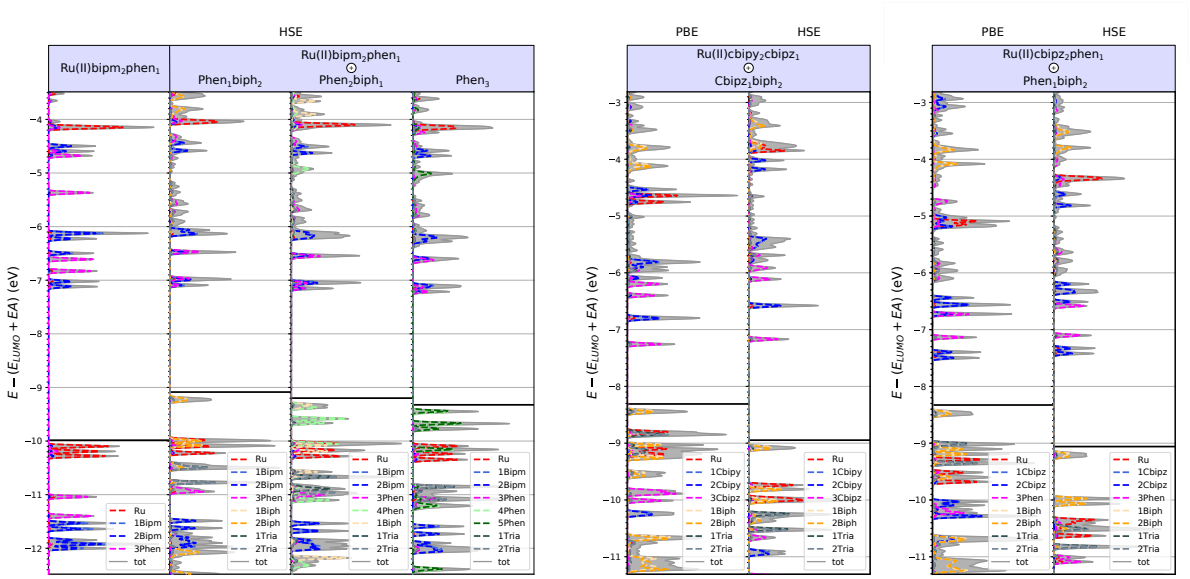

(a) (b) (c)

Figure S5: Densities of states calculated with the PBE and HSE06 functional (indicated at the top) for (Ru(II)bipm$_2$)phen$_1$(biph$_{3-n}$) ($n = 0, 1, 2$) (a), (Ru(II)cbipy$_2$)cbipz$_1$(biph$_2$) (b) and (Ru(II)cbipz$_2$)phen$_1$(biph$_2$) (c).

S4 The linkers

To examine the influence of including polypyridyl linkers/ligands in the CTF or Ru(II)L_3 complex, we first look at these isolated linkers. The linkers were modeled in the unit cell depicted in Figure S6.

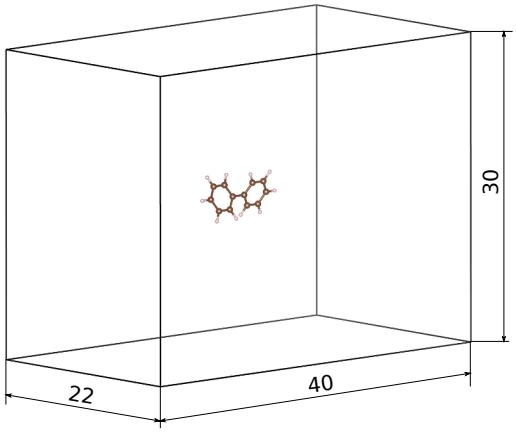

Figure S6: Dimensions (in Å) and orientation of the unit cell in which the linkers are calculated.

S4.1 Electronic structure

The electronic structure of both the CTFs and the Ru(II)L_3 complexes can to a large part be derived from the properties of the isolated linkers. The electronic structure of the isolated linkers is therefore examined by means of the density of states (DOS) aligned with respect to the vacuum level (Figure S7). In this way the energies of the highest occupied molecular orbital (HOMO) and lowest unoccupied orbital (LUMO) are a measure of the ionization energy and the electron affinity of the linker, respectively.

Figure S7 indicates that the LUMO lowers when more nitrogen atoms are present in the linker i.e. the electron affinity of the linker increases (see also Table S4). In contrast, the HOMO stays fairly constant, indicating a similar ionization energy across different linkers.

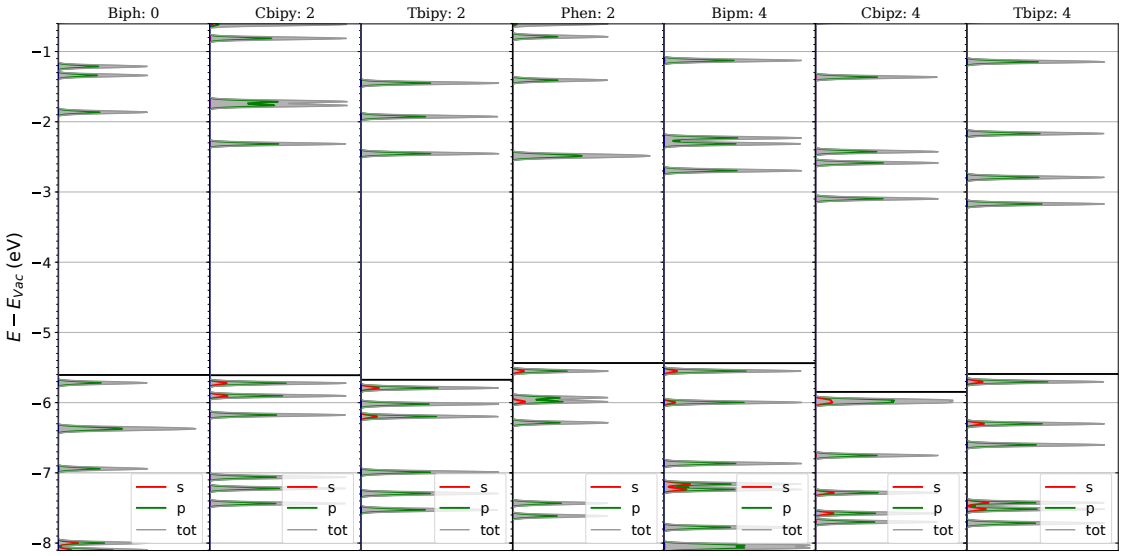

Figure S7: Densities of states of the linkers aligned with respect to the vacuum level. The DOS plots are ordered from low to high numbers of linker nitrogen atoms (indicated at the top).

L^i	Biph	Cbipy	Tbipy	Phen	Bipm	Cbipz	Tbipz
EA	0.258	0.471	0.548	0.599	0.670	0.941	0.991

Table S4: Electron affinities of the linkers (in eV), calculated as $EA = E[N] - E[N+1]$ with $E[N]$ the energy of the system with N electrons.

S5 The scaffold

As explained in the main article, the equilibrium surface is determined by uniformly rescaling the CTF's in-plane lattice parameters from -4% to 4% in steps of 1% and by fitting a Rose-Vinet equation of state[5] to the in-plane surface multiplied by the vacuum distance of 40 Å. An example for the $biph_3$ monolayer is shown in Figure S8.

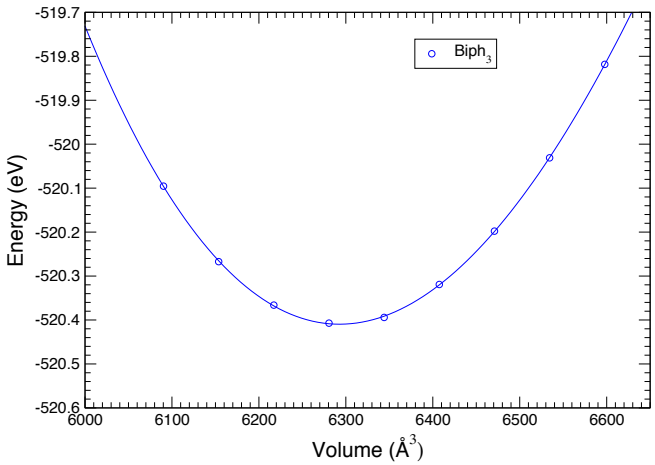

Figure S8: Example of a Rose-Vinet equation of state for the $biph_3$ CTF monolayer.

S5.1 Energetics

The formation energies of the CTFs are outlined in Table S5 (see Eq. 1 of the main article).

L^i	$L_1^i biph_2$	$L_2^i biph_1$	L_3^i
Biph	-11.294		
Cbipy	-9.465	-7.647	-5.822
Tbipy	-9.489	-7.670	-5.846
Phen	-9.491	-7.641	-5.897
Bipm	-9.546	-7.752	-5.910
Cbipz	-9.509	-7.709	-5.879
Tbipz	-9.505	7.714	-5.925

Table S5: Formation energies (in eV per unit cell) for the CTFs ($L_n^i biph_{3-n}, n = 0, 1, 2, 3$).

As outlined in Section of the main article the formation energy can be used to obtain the stabilization energy per linker, $\Delta E^{CTF}_{L^i(CN)}$, determined by a least-squares fit (see Eq. 1 of the main article). The results of this fit are tabulated in Tab S6.

L^i	Biph	Cbipy	Tbipy	Phen	Bipm	Cbipz	Tbipz
$\Delta E^{CTF}_{L^i(CN)}$	-3.769	-1.939	-1.949	-1.956	-1.979	-1.963	-1.974

Table S6: Decomposition of the CTF formation energy in stabilization energies per linker $\Delta E^{CTF}_{L^i(CN)}$ (in eV). The residual error of the least-squares fit is less than 3 meV.

S5.2 Electronic structure

The band gaps for the CTFs are summarized in Table S7. The electronic structures are shown in Figure S9.

L^i	$L^i_1 biph_2$	$L^i_2 biph_1$	L^i_3
Biph	2.57		
Cbipy	2.33	2.24	2.18
Tbipy	2.39	2.31	2.29
Phen	2.16	2.05	2.01
Bipm	1.89	1.75	1.69
Cbipz	2.13	1.97	1.90
Tbipz	1.84	1.65	1.63

Table S7: Band gaps (in eV) for the mixed-linker CTFs ($L^i_n biph_{3-n}, n = 0, 1, 2, 3$).

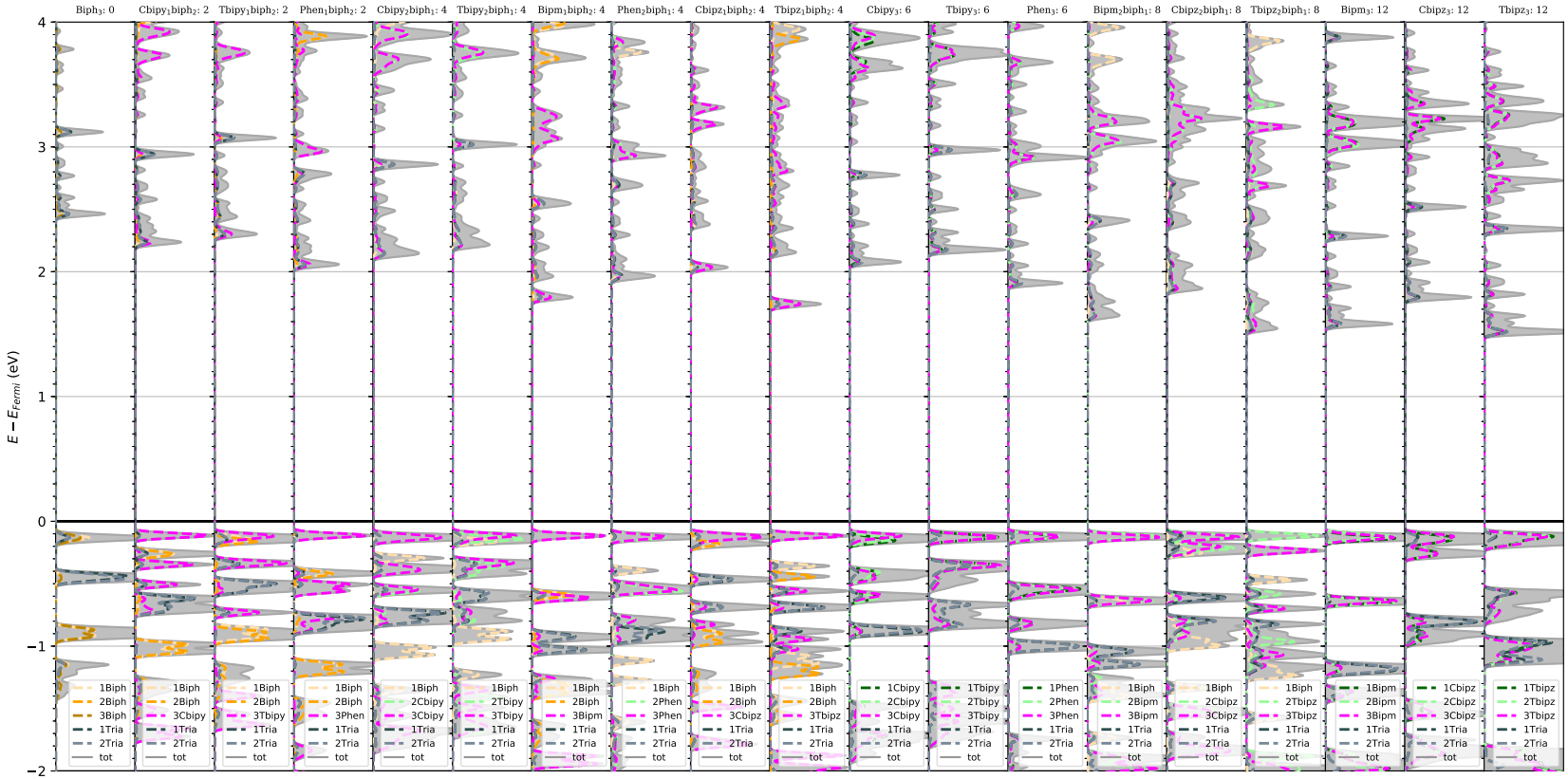

(a) Alignment based on the Fermi level

Figure S9: Densities of states of CTFs ($L_n^i biph_{3-n}, n = 0, 1, 2, 3$) for different alignment methods. The CTFs are ordered based on their number of linker nitrogen atoms (indicated at the top) and, when equal, based on the sum of electron affinities of their constituent linkers.

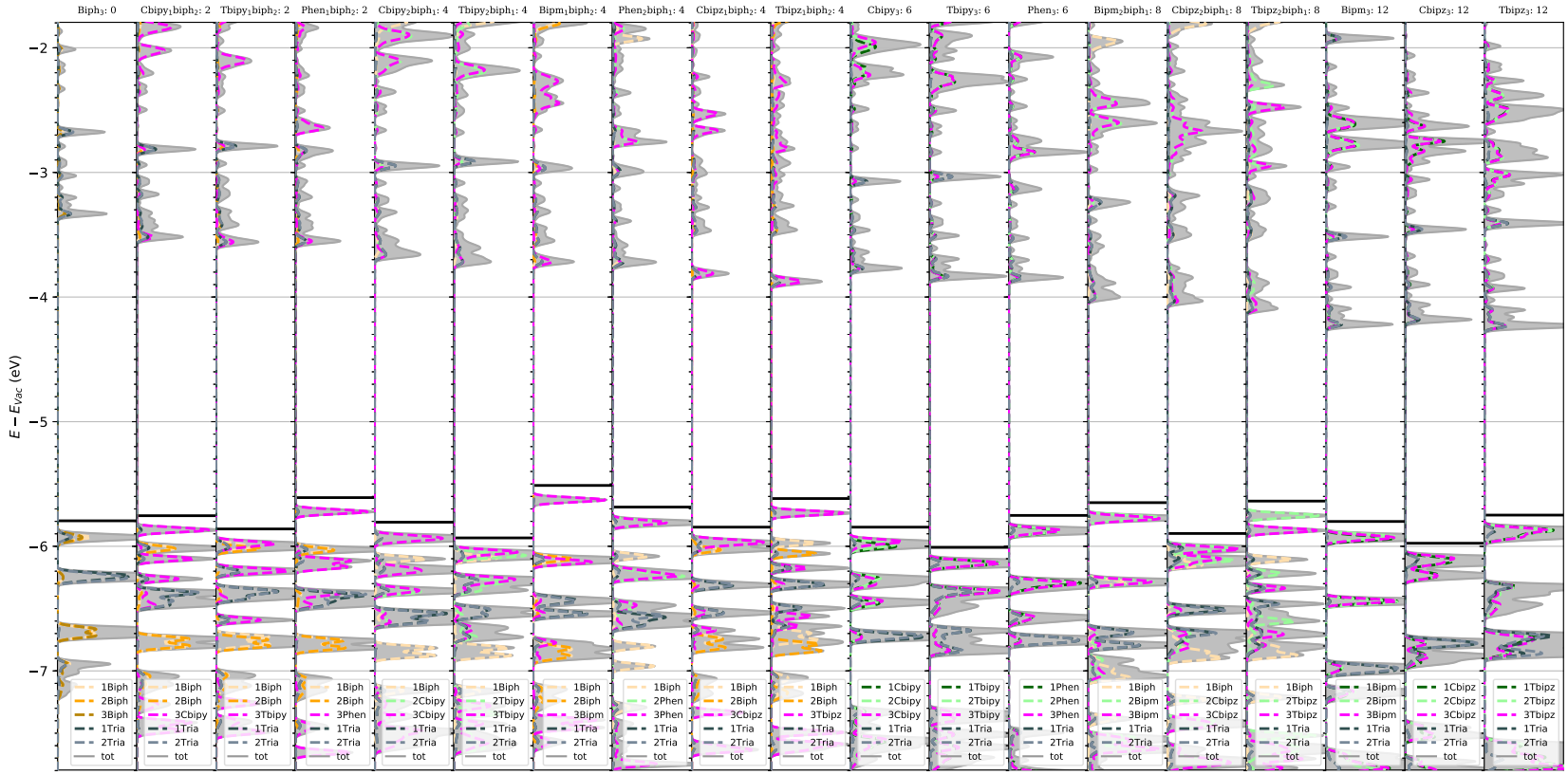

(b) Alignment based on the vacuum level

Figure S9: (continued) Densities of states of CTFs ($L_n^i biph_{3-n}, n = 0, 1, 2, 3$) for different alignment methods. The CTFs are ordered based on their number of linker nitrogen atoms (indicated at the top) and, when equal, based on the sum of electron affinities of their constituent linkers.

S6 The active complex

S6.1 Energetics

The formation energies of the Ru(II)L_3 complex are summarized in Table S8 (see Eq. 2 of the main article).

L_2^j \ L^i	Cbipy	Phen	Bipm	Cbipz
Cbipy	-22.915	-22.969	-22.487	-22.325
Phen	-23.020	-23.072	-22.606	-22.450
Bipm	-22.043	-22.109	-21.578	-21.380
Cbipz	-21.664	-21.739	-21.163	-20.933

Table S8: Formation energies (in eV) for the Ru(II)L_3 complexes (Ru(II)$L_2^jL_1^i$).

As outlined in Section of the main article, the formation energy can be used to obtain the stabilization energy per linker, $\Delta E^{Ru}_{\mathrm{L}^j(H)}$, determined by a least-squares fit (see Eq. 2 of the main article). The results of this fit are tabulated in Tab S9.

L^i	Cbipy	Phen	Bipm	Cbipz
$\Delta E^{Ru}_{\mathrm{L}^j(\mathrm{H})}$	-7.644	-7.702	-7.195	-6.997

Table S9: Decomposition of the formation energy of the Ru(II)L_3 complexes in stabilization energies per linker $\Delta E^{Ru}_{\mathrm{L}^j(\mathrm{H})}$ (in eV). The residual error of the least-squares fit is less than 4 meV.

S6.2 Electronic structure

In Figure S10 we compare how the electronic structure of the chelating ligands is transferred to the Ru(II)L_3 complex, using a qualitative alignment via the averaged core potential (see Section S2.2). There is a good resemblance between states centered on the chelating ligands and those of the isolated ligands, independent of the charge of the system.

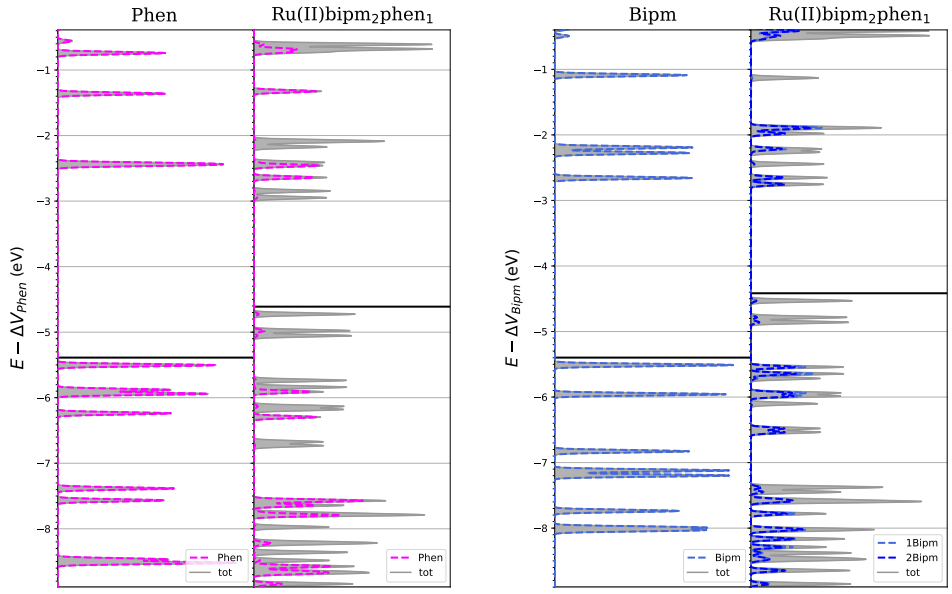

(a) Phen vs. Ru(II)bipm$_2$phen$_1$ (b) Bipm vs. Ru(II)bipm$_2$phen$_1$

Figure S10: Densities of states displaying how the properties of the chelating ligands are transferred to the Ru(II)L$_3$ complex. The electronic structures are aligned based on the average core potential of the biph linkers (a) or the Ru atom (b) respectively.

The values of the band gap and linker-linker gap for the Ru(II)L$_3$ complexes (see Figure 4b of the main article) are summarized in Table S10a and S10b, respectively. The electronic structures are shown in Figure S11.

L_2^j \ L^i	Cbipy	Phen	Bipm	Cbipz
Cbipy	1.82	1.83	1.76	1.76
Phen	1.85	1.87	1.83	1.76
Bipm	1.77	1.78	1.78	1.82
Cbipz	1.76	1.83	1.86	1.90

(a) Band gap

L_2^j \ L^i	Cbipy	Phen	Bipm	Cbipz
Cbipy	3.36	3.14	2.88	2.69
Phen	3.17	3.19	2.90	2.70
Bipm	2.78	2.79	2.69	2.58
Cbipz	2.55	2.56	2.51	2.39

(b) Linker-linker gap

Table S10: Band gaps (a) and linker-linker gaps (b) for the Ru(II)L$_3$ complexes Ru(II)L$_2^j$L$_1^i$ (in eV).

(a) Alignment based on the Fermi level

Figure S11: Densities of states of Ru(II)L_3 complexes (Ru(II)$L_2^jL_1^i$) for different alignment methods. The Ru(II)L_3 complexes are ordered based on their number of ligand nitrogen atoms (indicated at the top) and, when equal, based on the sum of electron affinities of their constituent ligands.

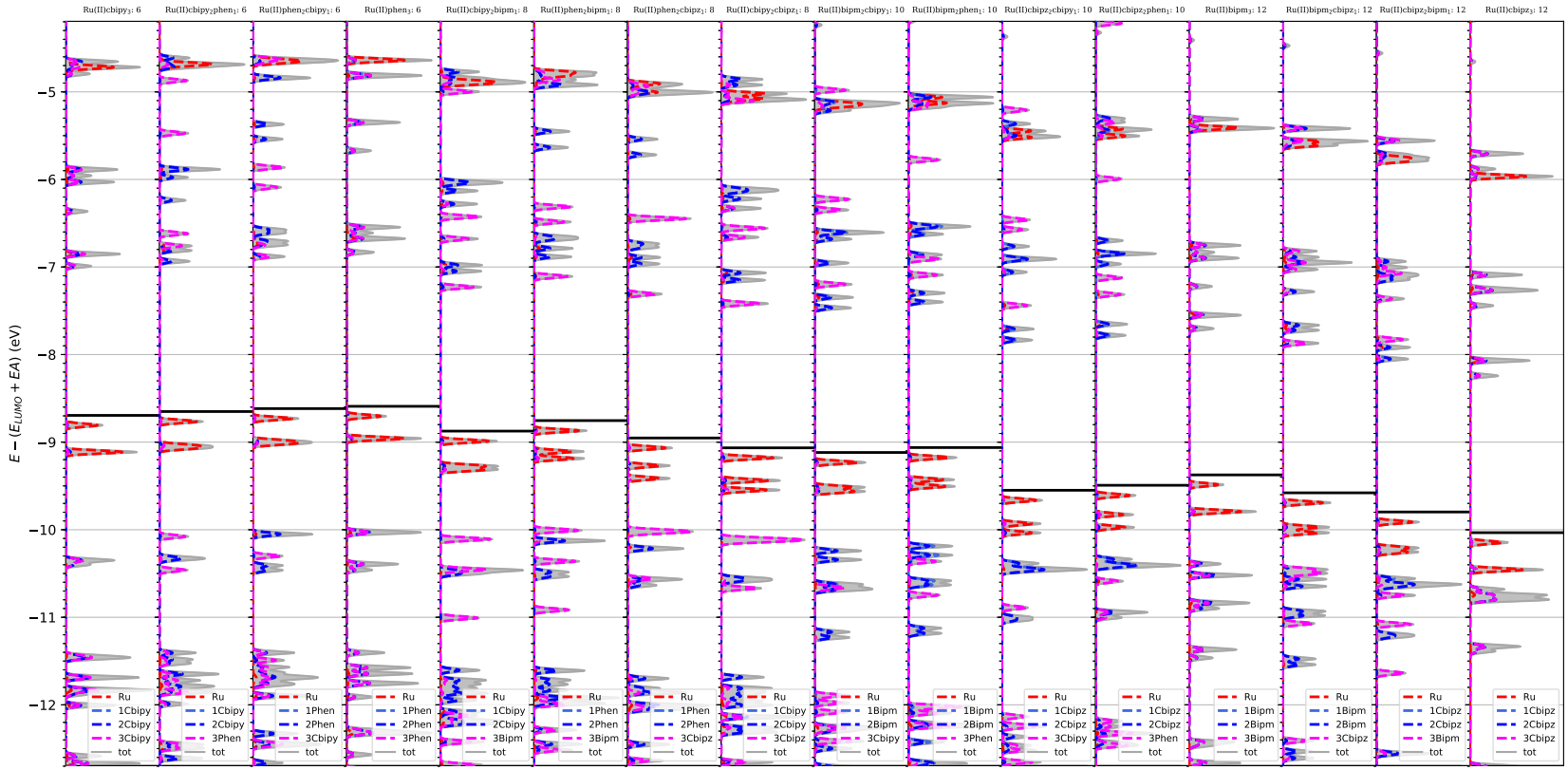

(b) Alignment based on the electron affinity

Figure S11: (continued) Densities of states of $Ru(II)L_3$ complexes ($Ru(II)L_2^jL_1^i$) for different alignment methods. The $Ru(II)L_3$ complexes are ordered based on their number of ligand nitrogen atoms (indicated at the top) and, when equal, based on the sum of electron affinities of their constituent ligands.

S7 The heterogeneous catalyst

S7.1 Energetics

The formation energies of the anchored Ru(II)L_3 complexes are summarized in Table S11 and Figure S12 (see Eq. 1 and Eq. 2 in the main article). Results are similar to those of the isolated components (see Figure 2 of the main manuscript).

L^i	Ru(II)cbipy$_2$L$_1^i$			Ru(II)phen$_2$L$_1^i$			Ru(II)bipm$_2$L$_1^i$			Ru(II)cbipz$_2$L$_1^i$		
	L_1^ibiph$_2$	L_2^ibiph$_1$	L_3^i	L_1^ibiph$_2$	L_2^ibiph$_1$	L_3^i	L_1^ibiph$_2$	L_2^ibiph$_1$	L_3^i	L_1^ibiph$_2$	L_2^ibiph$_1$	L_3^i
Cbipy	-32.916	-31.026	-29.144	-33.086			-32.144			-31.882	-29.979	-28.090
Phen	-33.063	-31.146	-29.250				-32.236	-30.342	-28.438	-31.997	-30.113	-28.191
Bipm	-32.722	-30.895	-29.032							-31.585	-29.635	-27.604
Cbipz	-32.450	-30.657	-28.799									

Table S11: Formation energies (in eV per unit cell) of the considered heterogeneous catalysts (Ru(II)L_2^j)L_1^i(L_n^ibiph$_{2-n}$) ($n = 0, 1, 2$).

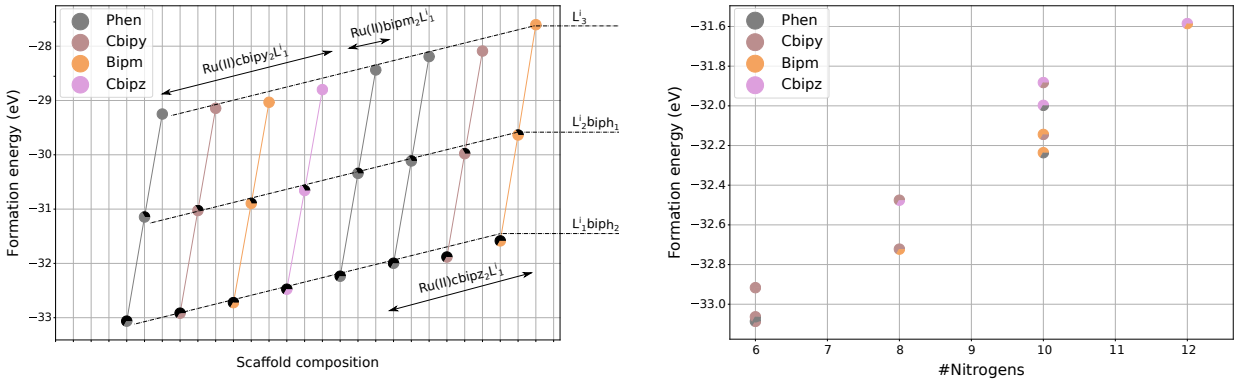

(a) Varying the CTF in CTF+Ru(II)L_3

(b) Varying Ru(II)L_3 in CTF+Ru(II)L_3

Figure S12: Formation energies (in eV per unit cell) of the Ru(II)L_3-CTF catalysts. Either the framework linkers can be altered while leaving the complex constant (a), or the Ru(II)L_3 complex ligands can be altered while keeping the non-anchoring linkers of the CTF scaffold constant at biph (b). Each data point is colored in three parts, which represent the composition of the CTF scaffold or Ru(II)L_3 complex, respectively. In panel (a) the solid lines connect all frameworks L_n^ibiph$_{3-n}$ with a fixed linker type L^i; the composition of the Ru(II)L_3 complex is indicated by means of arrows and the dashed lines correspond to different values of n.

As outlined in Section of the main article, the formation energy can be used to obtain stabilization energies per linker for pore ligands ($\Delta E^{het}_{L^j(H)}$), framework linkers ($\Delta E^{het}_{L^i(CN)}$) and the anchoring linker ($\Delta E^{het}_{L^i_{CTF-Ru}(CN)}$), by performing a least-squares fit (see Eq. 1 and Eq. 2 in the main article). The results of this fit are tabulated in Table S12.

L^i	Biph	Cbipy	Phen	Bipm	Cbipz
$\Delta E^{het}_{L^i(CN)}$	0 (0)	1.896 (1.829)	1.903 (1.812)	1.918 (1.790)	1.824 (1.805)
$\Delta E^{het}_{L^j(H)}$	N.A.	0.060 (0.058)	0 (0)	0.480 (0.507)	0.622 (0.705)
$\Delta E^{het}_{L^i_{CTF-Ru}(CN)}$	N.A.	0.122	0	0.364	0.629

Table S12: Stabilization energies per linker (in eV) for pore ligands $\Delta E^{het}_{L^j(H)}$, framework linkers $\Delta E^{het}_{L^i(CN)}$ and the anchoring linker $\Delta E^{het}_{L^i_{CTF-Ru}(CN)}$ relative to the lowest energy in their respective class (pore, framework or anchoring linker). The corresponding relative stabilization energies of the CTF and Ru(II)L_3 linkers/ligands are given between brackets (see Table S6 and S9). The residual error of the least-squares fit is equal to 3 meV.

We also calculated anchoring energies. The process to anchor a Ru(II)L^j_3 complex onto the L^i_{CTF-Ru} linker of the $L^i_{n+1}biph_{2-n}$ CTF ($n = 0, 1, 2$) corresponds to the following reaction:

$$L^i_{n+1}\text{biph}_{2-n} + \text{Ru(II)}L^j_3 \longrightarrow (\text{Ru(II)}L^j_2)L^i_1(L^i_n\text{biph}_{2-n}) + L^j \tag{S2}$$

The energy needed form the $(\text{Ru(II)}L^j_2)L^i_1(L^i_n\text{biph}_{2-n})$ catalyst through anchoring can thus be calculated as

$$\begin{aligned}\Delta E_a &= E[(\text{Ru(II)}L^j_2)L^i_1(L^i_n\text{biph}_{2-n})] + E[L^j] - E[L^i_{n+1}\text{biph}_{2-n}] - E[\text{Ru(II)}L^j_3] \\ &= E_{Form}[(\text{Ru(II)}L^j_2)L^i_1(L^i_n\text{biph}_{2-n})] - E_{Form}[\text{Ru(II)}L^j_3] - E_{Form}[L^i_{n+1}\text{biph}_{2-n}],\end{aligned} \tag{S3}$$

for which the values are summarized in Table S13.

L^i	Ru(II)cbipy$_2L^i_1$			Ru(II)phen$_2L^i_1$			Ru(II)bipm$_2L^i_1$			Ru(II)cbipz$_2L^i_1$		
	L^i_1biph$_2$	L^i_2biph$_1$	L^i_3	L^i_1biph$_2$	L^i_2biph$_1$	L^i_3	L^i_1biph$_2$	L^i_2biph$_1$	L^i_3	L^i_1biph$_2$	L^i_2biph$_1$	L^i_3
Cbipy	-0.536	-0.464	-0.407	-0.549			-1.101			-1.484	-1.399	-1.335
Phen	-0.657	-0.590	-0.438				-1.167	-1.123	-0.963	-1.573	-1.539	-1.361
Bipm	-0.261	-0.228	-0.207							-1.106	-0.950	-0.761
Cbipz	-0.026	-0.033	-0.005									

Table S13: Anchoring energy (in eV), corresponding to the attachment of a Ru(II)L^j_3 complex onto the L^i_{CTF-Ru} linker of a $L^i_{n+1}\text{biph}_{2-n}$ CTF, forming the $(\text{Ru(II)}L^j_2)L^i_1(L^i_n\text{biph}_{2-n})$ catalyst.

S7.2 Electronic structure

Figure S13 shows how the electronic structure of the Ru(II)L_3-CTF heterogeneous catalyst is inherited from the CTF and Ru(II)L_3 complex, using a qualitative alignment via the average core potential (see Section S2.2). It indicates a strong resemblance between states of the catalyst centered on the framework with those in the sole scaffold. Similarly, states centered on constituents of the Ru(II)L_3 complex in the catalyst resemble those of the corresponding isolated Ru(II)L_3 complex.

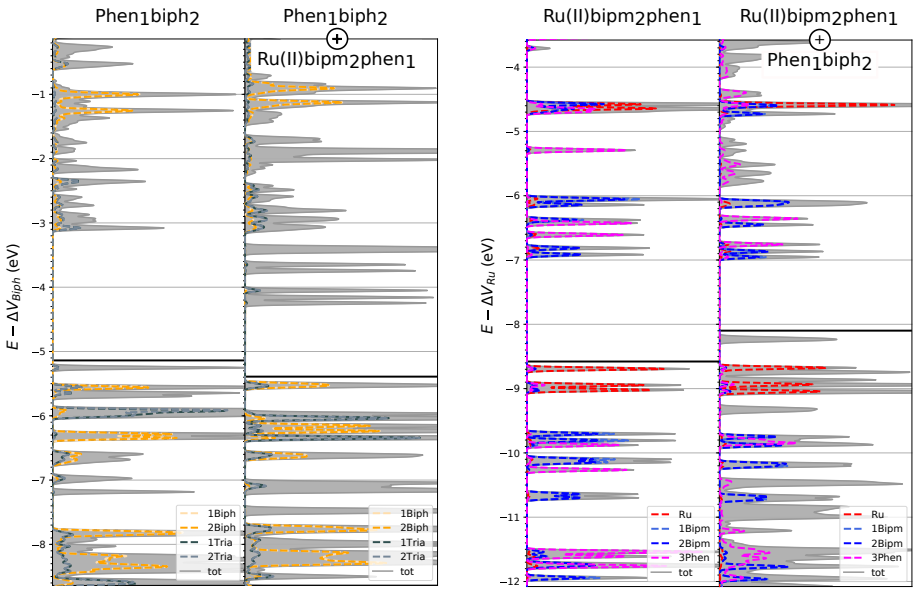

(a) CTF vs. CTF+Ru (b) Ru vs. CTF+Ru

Figure S13: Densities of states displaying how the properties of the CTF (a) and the Ru(II)L_3 complex (b) are transferred to the combined Ru(II)L_3-CTF heterogeneous catalyst. The electronic structures are aligned based on the average core potential of the biph linkers (a) or the Ru atom (b), respectively.

The values of the band gap for all calculated Ru(II)L_3-CTF catalyst are summarized in Table S14. The electronic structures are shown in Figure S14 and Figure S15.

L^i	Ru(II)cbipy$_2$L$_1^i$			Ru(II)phen$_2$L$_1^i$			Ru(II)bipm$_2$L$_1^i$			Ru(II)cbipz$_2$L$_1^i$		
	L_1^ibiph$_2$	L_2^ibiph$_1$	L_3^i	L_1^ibiph$_2$	L_2^ibiph$_1$	L_3^i	L_1^ibiph$_2$	L_2^ibiph$_1$	L_3^i	L_1^ibiph$_2$	L_2^ibiph$_1$	L_3^i
Cbipy	1.515	1.253	1.228	1.549			1.211			0.928	0.639	0.648
Phen	1.603	1.893	1.192				1.252	0.869	0.903	0.942	0.509	0.538
Bipm	1.308	0.804	0.816							0.862	0.376	0.428
Cbipz	1.161	0.966	0.952									

Table S14: Band gaps (in eV) for the considered catalysts (Ru(II)L$_2^j$)L$_1^i$(L$_n^i$biph$_{2-n}$).

Figure S14 displays how the electronic structure is altered if the chelating ligands of the anchored Ru(II)L_3 complex are varied. It indicates how one could tune the MLCT of the anchored Ru(II)L_3 complex.

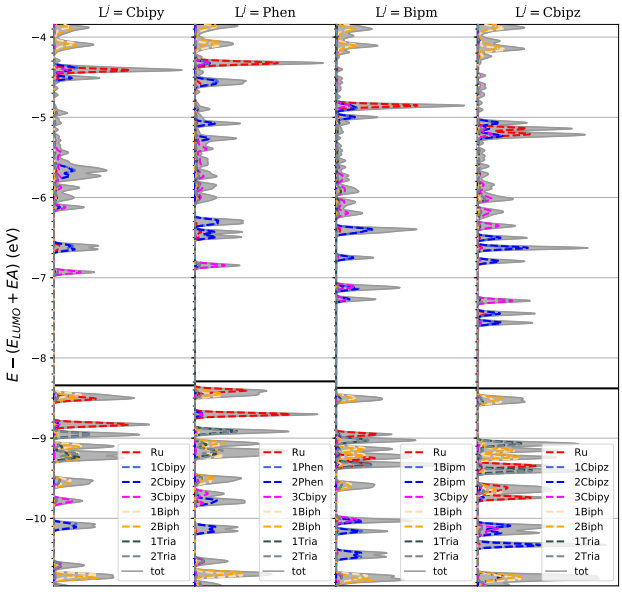

(a) $(\mathrm{Ru(II)L}_2^j)\mathrm{cbipy}_1(\mathrm{biph}_2)$

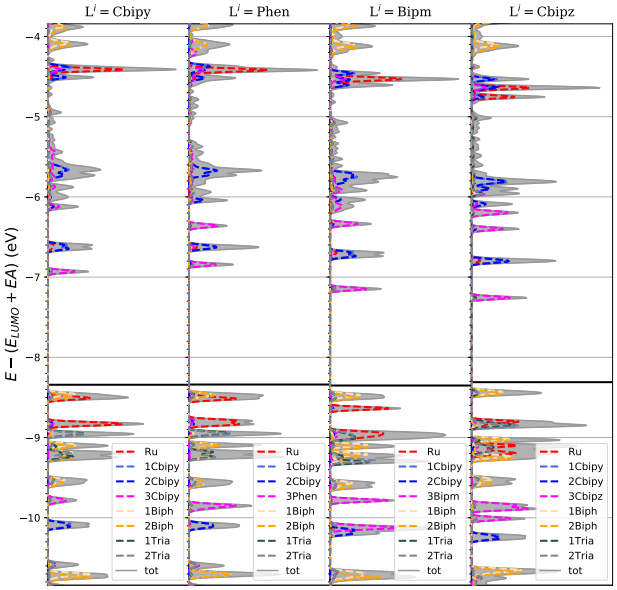

(b) $(\mathrm{Ru(II)cbipy}_2)\mathrm{L}_1^i(\mathrm{biph}_2)$

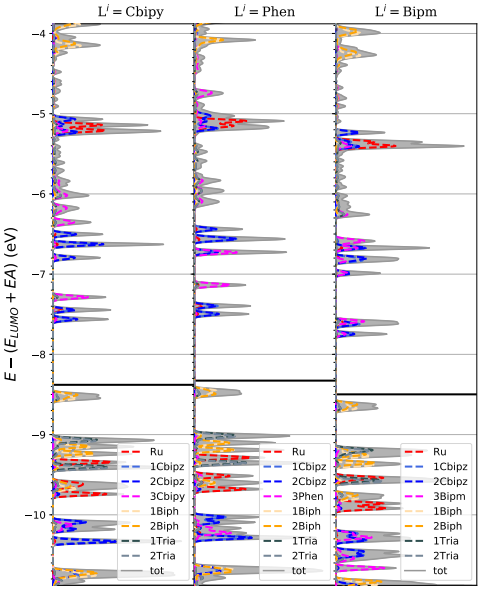

(c) $(\mathrm{Ru(II)cbipz}_2)\mathrm{L}_1^i(\mathrm{biph}_2)$

Figure S14: Densities of states indicating the possibility of guiding the MLCT, characterized by the LUMO state, towards the pore (blue) or framework (magenta) by altering the ligands surrounding the $\mathrm{Ru(II)L}_3$ complex.

Figure S15 on the other hand indicates how the electronic properties of the $\mathrm{Ru(II)L}_3$ complex are transferred to the catalyst. The electronic structures are aligned based on the electron affinity. These plots therefore indicate that the chemical activity of the complexes stays intact. However it is found that there is some influence through the nitrogen content of the framework, as can be seen

in the right panel of every subfigure when going from left to right, i.e. by increasing the number of nitrogeneous linkers in the framework.

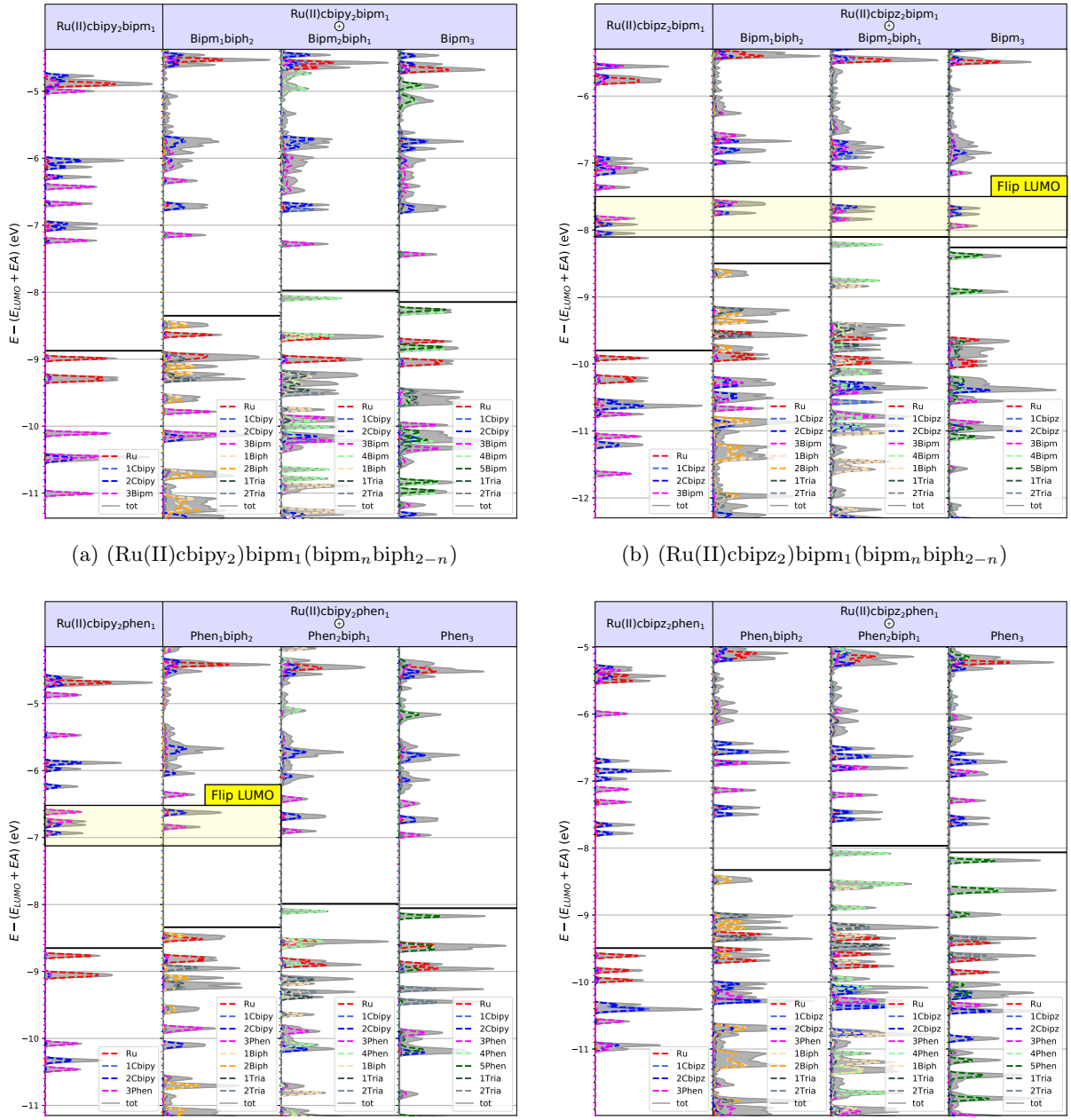

(a) $(\mathrm{Ru(II)cbipy_2})\mathrm{bipm_1}(\mathrm{bipm}_n\mathrm{biph}_{2-n})$

(b) $(\mathrm{Ru(II)cbipz_2})\mathrm{bipm_1}(\mathrm{bipm}_n\mathrm{biph}_{2-n})$

(c) $(\mathrm{Ru(II)cbipy_2})\mathrm{phen_1}(\mathrm{phen}_n\mathrm{biph}_{2-n})$

(d) $(\mathrm{Ru(II)cbipz_2})\mathrm{phen_1}(\mathrm{phen}_n\mathrm{biph}_{2-n})$

Figure S15: Densities of states displaying how the properties of the $\mathrm{Ru(II)L_3}$ complex are transferred to the $\mathrm{Ru(II)L_3}$-CTF heterogeneous catalyst when anchored. The effect of the nitrogen content of the CTF on the $\mathrm{Ru(II)L_3}$ complexes states is also shown in each subfigure (a)-(g).

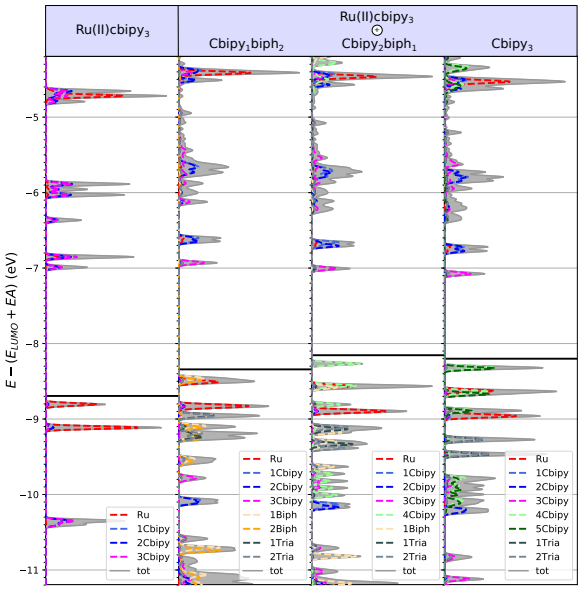

(e) $(\mathrm{Ru(II)cbipy_2})\mathrm{cbipy}(\mathrm{cbipy}_n\mathrm{biph}_{2-n})$

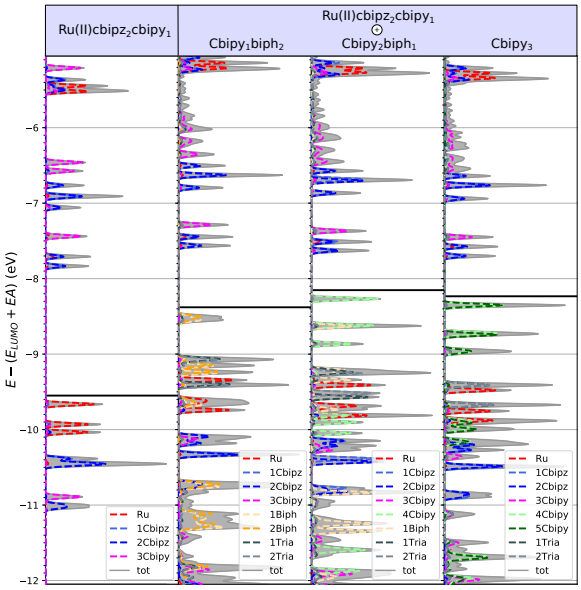

(f) $(\mathrm{Ru(II)cbipz_2})\mathrm{cbipy_1}(\mathrm{cbipy}_n\mathrm{biph}_{2-n})$

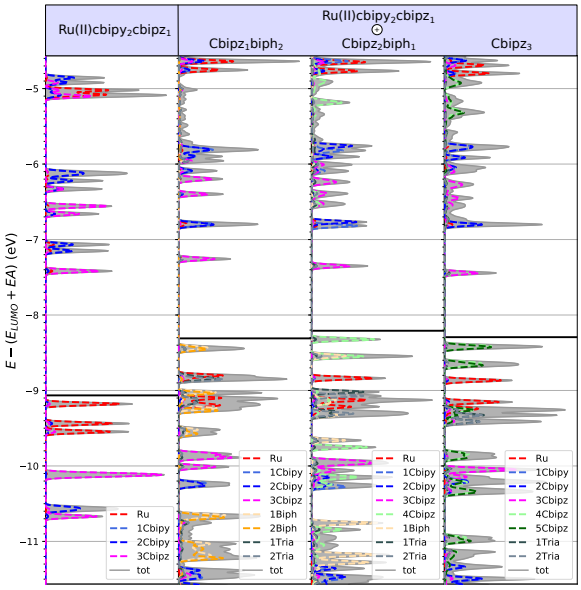

(g) $(\mathrm{Ru(II)cbipy_2})\mathrm{cbipz_1}(\mathrm{cbipz}_n\mathrm{biph}_{2-n})$

Figure S15: (continued) Densities of states displaying how the properties of the $\mathrm{Ru(II)L_3}$ complex are transferred to the $\mathrm{Ru(II)L_3}$-CTF heterogeneous catalyst when anchored. The effect of the nitrogen content of the CTF on the $\mathrm{Ru(II)L_3}$ complexes states is also shown in each subfigure (a)-(g).

References

(1) Leslie, M.; Gillan, N. J. *J. Phys. C: Solid State Phys.* **1985**, *18*, 973.

(2) Frisch, M. J.; Trucks, G. W.; Schlegel, H. B.; Scuseria, G. E.; Robb, M. A.; Cheeseman, J. R.; Scalmani, G.; Barone, V.; Petersson, G. A.; Nakatsuji, H.; Li, X.; Caricato, M.; Marenich, A. V.; Bloino, J.; Janesko, B. G.; Gomperts, R.; Mennucci, B.; Hratchian, H. P.; Ortiz, J. V.; Izmaylov, A. F.; Sonnenberg, J. L.; Williams-Young, D.; Ding, F.; Lipparini, F.; Egidi, F.; Goings, J.; Peng, B.; Petrone, A.; Henderson, T.; Ranasinghe, D.; Zakrzewski, V. G.; Gao, J.; Rega, N.; Zheng, G.; Liang, W.; Hada, M.; Ehara, M.; Toyota, K.; Fukuda, R.; Hasegawa, J.; Ishida, M.; Nakajima, T.; Honda, Y.; Kitao, O.; Nakai, H.; Vreven, T.; Throssell, K.; Montgomery, J. A., Jr.; Peralta, J. E.; Ogliaro, F.; Bearpark, M. J.; Heyd, J. J.; Brothers, E. N.; Kudin, K. N.; Staroverov, V. N.; Keith, T. A.; Kobayashi, R.; Normand, J.; Raghavachari, K.; Rendell, A. P.; Burant, J. C.; Iyengar, S. S.; Tomasi, J.; Cossi, M.; Millam, J. M.; Klene, M.; Adamo, C.; Cammi, R.; Ochterski, J. W.; Martin, R. L.; Morokuma, K.; Farkas, O.; Foresman, J. B.; Fox, D. J. Gaussian 16 Revision B.01. 2016; Gaussian Inc. Wallingford CT.

(3) Weigend, F. *Phys. Chem. Chem. Phys.* **2006**, *8*, 1057–1065.

(4) Weigend, F.; Ahlrichs, R. *Phys. Chem. Chem. Phys.* **2005**, 3297–3305.

(5) Vinet, P.; Ferrante, J.; Rose, J. H.; Smith, J. R. *J. Geophys. Res. Solid Earth* **1987**, *92*, 9319–9325.